

1 **Current potential of CH₄ emission estimates using TROPOMI in the Middle East**

2
3 Mengyao Liu^{1*}, Ronald van der A¹, Michiel van Weele¹, Lotte Bryan^{1,2}, Henk Eskes¹,
4 Pepijn Veefkind^{1,2}, Yongxue Liu³, Xiaojuan Lin^{1,4}, Jos de Laat¹, Jieying Ding¹

5 ¹ KNMI, Royal Netherlands Meteorological Institute, De Bilt, The Netherlands

6 ² Delft University of Technology, Delft, The Netherlands

7 ³ School of Geographic and Oceanographic Sciences, Nanjing University, Nanjing,
8 China

9 ⁴ Department of Earth System Science, Ministry of Education Key Laboratory for Earth
10 System Modeling, Tsinghua University, Beijing, China

11 * Correspondence to: Mengyao Liu (mengyao.liu@knmi.nl)

12 **Abstract**

13 An improved divergence method has been developed to estimate annual methane (CH₄)
14 emissions from TROPOspheric Monitoring Instrument (TROPOMI) observations. It
15 has been applied to the period of 2018 to 2021 over the Middle East, where the
16 orography is complicated, and the mean mixing ratio of methane (XCH₄) might be
17 affected by albedos or aerosols over some locations. To adapt to extreme changes of
18 terrain over mountains or coasts, winds are used with their divergent part removed. A
19 temporal filter is introduced to identify highly variable emissions and further exclude
20 fake sources caused by retrieval artifacts. We compare our results to widely used
21 bottom-up anthropogenic emission inventories: Emissions Database for Global
22 Atmospheric Research (EDGAR), Community Emissions Data System (CEDS) and
23 Global Fuel Exploitation Inventory (GFEI) over several regions representing various
24 types of sources. The NO_x emissions from EDGAR and Daily Emissions Constrained
25 by Satellite Observations (DECOS), and the industrial heat sources identified by Visible
26 Infrared Imaging Radiometer Suite (VIIRS) are further used to better understand our
27 resulting methane emissions. Our results indicate possibly large underestimations of
28 methane emissions in metropolises like Tehran (up to 50%) and Isfahan (up to 70%) in
29 Iran. The derived annual methane emissions from oil/gas production near the Caspian
30 Sea in Turkmenistan are comparable to GFEI but more than two times higher than
31 EDGAR and CEDS in 2019. Large discrepancies of distribution of methane sources in
32 Riyadh and its surrounding areas are found between EDGAR, CEDS, GFEI and our

33 emissions. The methane emission from oil/gas production in the east to Riyadh seems
34 to be largely overestimated by EDGAR and CEDS, while our estimates, and also GFEI
35 and DECSO NO_x indicate much lower emissions from industry activities. On the other
36 hand, regions like Iran, Iraq, and Oman are dominated by sources from oil and gas
37 exploitation that probably includes more irregular releases of methane, with the result
38 that our estimates, that include only invariable sources, are lower than the bottom-up
39 emission inventories.

40 1 Introduction

41 Methane (CH₄) is the second most important greenhouse gas of which the abundance
42 kept increasing in the last decades (Turner et al., 2019; Saunio et al., 2020; Eyring et
43 al., 2021), with a short-term stable concentration level between the years 2000 and 2006
44 (Dlugokencky et al., 2009; Rigby et al., 2008). The relatively short lifetime of about a
45 decade makes CH₄ emissions a short-term target for mitigating climate change. The
46 TROPospheric Monitoring Instrument (TROPOMI) on board the Sentinel 5 Precursor
47 (S5-P) satellite provides an opportunity to measure CH₄ globally at a high resolution of
48 7×7 km² since its launch in October 2017 (upgraded to 5.5×7 km² in August 2019)
49 (Veefkind et al., 2012; Lorente et al., 2021). Previous studies have demonstrated the
50 capability of TROPOMI to identify big CH₄ emitters (e.g., leakages from pipelines)
51 through detecting large anomalies or to derive regional emission fields (de Gouw et al.,
52 2020; Pandey et al., 2019; Zhang et al., 2020; Chen et al., 2023).

53 However, using observations from TROPOMI to quantify emissions are also facing
54 challenges. On the one hand, some sources are located near the coast or in places with
55 complex topography, where satellite observations are often of reduced quality. The
56 observations of TROPOMI CH₄ contain uncertainties from retrieval assumptions for
57 surface albedo, aerosols, and the sun-glint model over the ocean. On the other hand, the
58 characteristics of the various sources are poorly understood. For instance, constant
59 emitting sources from landfills *versus* intermittent leakage of oil/gas, makes it difficult
60 to quantify their emissions (Varon, 2021).

61 The Middle East is one of the strong CH₄-emitting regions in the world (Chen et al.,
62 2023). Nevertheless, these emissions are particularly challenging to be quantified
63 because of the aspects aforementioned. Lauvaux et al. (2022) found fewer detections
64 of ultra-emitters (>25 kg/hour) in Middle Eastern countries like Iraq, Saudi Arabia than
65 other hot-spot regions like the U.S. from TROPOMI observations. Chen et al., (2023)
66 also revealed large discrepancies between a priori and posterior emission inventory
67 derived from satellites over the Middle East.

68 In this study, we present an improved divergence method (Beirle et al., 2019, [2023](#); Liu
69 et al., 2021; [Sun et al., 2022](#); Veefkind., 2023) to quantify the emissions of CH₄ over
70 the Middle East from 2018 to 2021 on a grid of 0.2° from TROPOMI retrieved XCH₄
71 by using the latest version of the scientific retrieval product (TROPOMI/WFMD v1.8)
72 from the University of Bremen (Schneising et al., 2023). This inversion algorithm is
73 based on the mass balance theory and is unique because of its speed and no need for a
74 priori knowledge of the sources. The wind divergence was first removed from the daily
75 wind fields to better adapt to the complicated orography in the Middle East, and a
76 temporal filter was developed in this study to exclude incorrect sources caused by
77 retrieval issues, respectively. For an area without influence from retrieval issues (e.g.,
78 albedo), the persistence of sources can be further tested by the temporal filter.

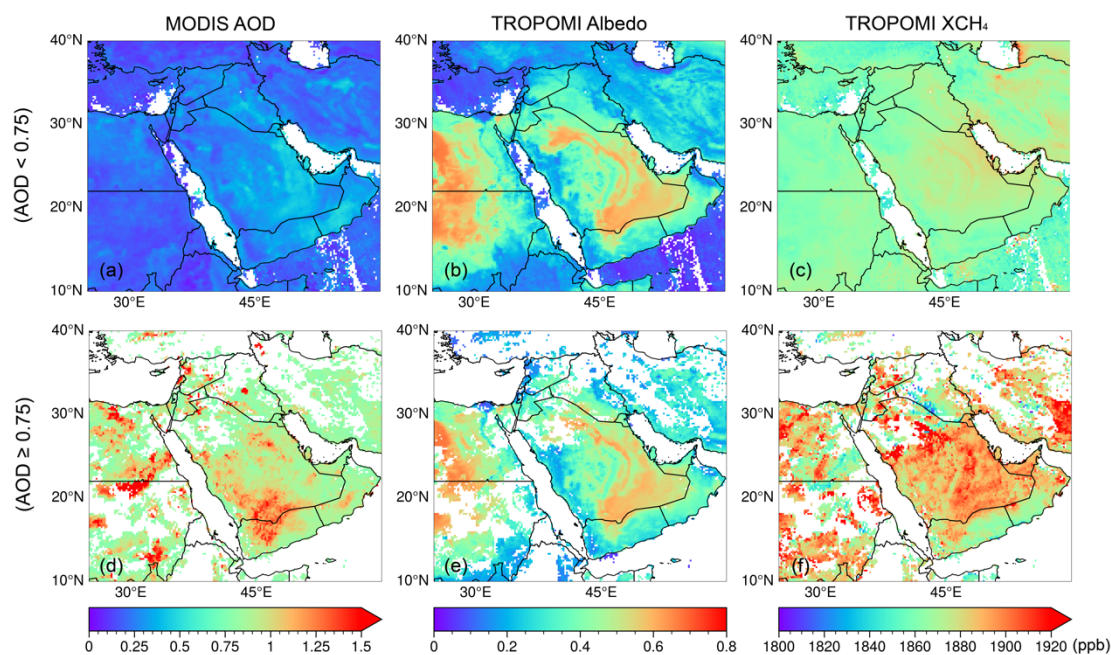
79 Before calculating the divergence, we exclude contaminated pixels with a high aerosol
80 optical depth (AOD) using daily MODIS AOD observations and the global hourly
81 Atmospheric Composition Reanalysis 4 (EAC4) dataset. To a grid cell that shows a
82 strong spatial correlation between the divergence and its corresponding background
83 divergence, a posterior correction is applied to remove the contribution from the
84 inhomogeneous background. The final results are further compared to the total
85 anthropogenic CH₄ emissions from Emissions Database for Global Atmospheric
86 Research (EDGAR) v7.0 (Crippa et al., 2022) and CEDS v_2021_04_21 (O'Rourke et
87 al., 2021). Other auxiliary datasets, such as the methane emissions from the fuel
88 exploitation predicted by GEFI v2 (Scarpelli et al., 2019) and total anthropogenic NO_x
89 emissions from EDGAR v6.1 and DECSO v6.2 (van der A et al., 2024; Ding et al.,
90 2020; Mijling and van der A, 2012) are used for a better interpretation of our results.

91 **2 Data and Methodology**

92 *2.1 Selection of reliable TROPOMI XCH₄ data*

93 This study used the latest TROPOMI WFM-DOAS (TROPOMI/WFMD v1.8) XCH₄
94 product (Schneising et al., 2023). Quality filters were applied to reduce the size of a
95 daily XCH₄ file before making it available to the public. Thus, the daily files contain
96 only the pixels that had passed the quality check. In version 1.8, a de-stripping filter has
97 been applied to each orbit.

98 The TROPOMI/WFMD algorithm has been designed for clear-sky scenes with minor
99 scattering by aerosols and optically thin clouds (i.e., cirrus). Still, a few pixels could
100 contain high aerosol loadings (MODIS AOD at 550 nm ≥ 0.75 , Fig. 1. d–f v.s. a–c),
101 leading to biased high XCH₄. We here use the daily observation of 10 km MODIS/Aqua
102 AOD data at 550 nm, which has a similar overpass time as TROPOMI, to estimate the
103 AOD values for pixels of TROPOMI. The pixels with AOD ≥ 0.75 are filtered, and 1.7%
104 of pixels in 2019 are excluded with this criterion in the domain of 10–40N°, 20–50E°.
105 Admittedly, not every TROPOMI pixel has a collocated MODIS AOD observation.
106 Thus, we used the global hourly EAC4 dataset combined with MODIS daily
107 observations to ensure every pixel of TROPOMI has an AOD estimate to reduce the
108 systematic biases caused by high aerosol loadings while maintaining as many pixels as
109 possible. The details about obtaining an AOD value for each pixel can be found in Part
110 A of the Supplementary Information (SI).



111

112 **Figure 1.** Annual mean of (a) MODIS AOD, (b) albedo in TROPOMI XCH4 retrieval
 113 and (c) TROPOMI XCH4 on a grid of 0.2° in 2019, which are the average of pixels
 114 with $AOD < 0.75$. (d)-(f) are similar to (a)-(c) but based on the pixels with $AOD \geq 0.75$.
 115 Only pixels with available MODIS AOD are used to generate the maps shown here.

116 Another aspect that is addressed is the distinction between land and water bodies,
 117 especially over the coastlines. TROPOMI use different retrieval strategies for data over
 118 land and ocean. The retrievals over ocean are only available in sun glint mode. We find
 119 the data over ocean can be quite noisy. Furthermore, the data continuous from land to
 120 ocean are checked. We selected pixels locating at several $1^\circ \times 1^\circ$ areas covering half
 121 land and half ocean at the coastlines of Oman, Yemen and along the Red Sea. We found
 122 there are not many differences between pixels over land and ocean (see Figure S1 in
 123 SI). Therefore, we built a water-land mask at the same spatial resolution as our emission
 124 data ($0.2^\circ \times 0.2^\circ$) based on Global Land Cover Characterization (GLCC) of the United
 125 States Geological Survey (USGS) (United States Geological Survey, 2018a, b) to
 126 distinguish water, land and the coast (transition grids from land to water). Only grid
 127 cells that are marked as land and coast are used to build the regional background and
 128 are used to calculate the daily divergence.

129 2.2 Methane bottom-up emission inventories and auxiliary emission datasets

130 In this study, EDGAR v7.0 is mainly used to evaluate the result of the derived methane
 131 emissions because it covers the whole period of our study. EDGARv7.0 provides
 132 estimates for emissions of the three main greenhouse gases (CO_2 , CH_4 , N_2O) per sector
 133 and country from 1970 to 2021 on a grid of 0.1° . The activity data for non- CO_2
 134 emissions are primarily based on the World Energy Balances data (2021) of the IEA.

135 The activity data for certain sectors are further modified by other updated datasets. For
136 example, International Fertiliser Association (IFA) and Gas Flaring Reduction
137 Partnership (GGFR)/U.S. National Oceanic and Atmospheric Administration (NOAA),
138 United Nations Framework Convention on Climate Change (UNFCCC) and World
139 Steel Association (worldsteel) recent statistics are used for activity data of energy-
140 related sectors, and agricultural sectors are further modified by FAO (2021). In addition,
141 the latest version (v_2021_04_21) of CEDS and the Global Fuel Exploitation Inventory
142 (GFEI v2) are also used for comparisons in specific years. CEDS v_2021_04_21
143 consists of CMIP6 historical anthropogenic emissions data from 1980 - 2019 on a grid
144 of 0.5°. The 0.5° data was further downscaled to 0.1° using 0.1° proxy data from
145 EDGAR v5.0 emission grids (O'Rourke et al., 2021). GFEI v2 allocates methane
146 emissions from oil, gas, and coal to a grid of 0.1° by using the national emissions
147 reported by individual countries to UNFCCC and assign them to infrastructure
148 locations. GFEI v2 inventory is available for 2019 and presents an update of GFEI v1
149 which was made for 2016 (Scarpelli, et al., 2021).

150 Despite the fact that the three above-mentioned inventories have assembled various
151 information from recent statistics, emissions in the Middle East are still uncertain and
152 show large discrepancies because of the lack of reports from the industrial facilities. To
153 validate the sources not reported in bottom-up inventories, target-mode instruments
154 with very high spatial resolution (pixels < 60m) (e.g., GHGSat, PRISMA, EMIT) are
155 widely used to pinpoint individual sources and reveal their characteristics. NASA's
156 Earth Surface Mineral Dust Source Investigation (EMIT) mission was launched in 2020
157 and methane plumes are recorded since 10th August 2022 (Source:
158 <https://earth.jpl.nasa.gov/emit/data/data-portal/Greenhouse-Gases/>). It uses an
159 advanced imaging spectrometer instrument that measures a spectrum for every point in
160 the image. The high-confidence research grade methane plume complexes from point
161 source emitters are released as they are identified (Brodrick et al., 2023). In addition,
162 NO_x emissions and gas flaring data are often used to analyze the emission of methane,
163 especially for the energy-related sources. Thus, we further used NO_x emissions and
164 industrial heat sources identified by VIIRS (Liu et al., 2018) to better understand the
165 derived methane emissions. The latest NO_x emissions from EDGAR (v6.1, the most
166 recent year is 2018) and the top-down NO_x emission inventory from TROPOMI,
167 DECSO (van der A et al., 2023; Ding et al., 2020), are used to assesseess uncertainties
168 of various emission inventories. For clarity, we combined the source sectors of methane
169 in EDGAR and CEDS, and the sectors of NO_x in EDGAR into two categories: energy
170 and others. The sectors for each category are listed in Table-1.

171

Table 1. Sectors of CH₄ and NO_x used in this study based on EDGAR

Sector Species	Energy	Others
¹ EDGAR v7.0 CH ₄	1, Power industry (1A1a) 2, Refineries and transformation industry (1A1b+1A1ci+1A1cii+1A5biii+1B1b+1B2aiii6+1B2biii3+1B1c) 3, Combustion for manufacturing (1A2) 4, Fuel exploitation (1B1a+1B2aiii2+1B2aiii3+1B2bi+1B2bi i) 5, Chemistry process (2B) 6, Energy for building (1A4 +1A5) 7, Iron and steel production (2C2) 8, Fossil fuel fires (5B)	Transportation 1, Aviation (1A3a) 2, Railways, pipelines, off-road transport (1A3c+1A3e) 3, Shipping (1A3d) Agricultural 1, Manure management (3A2) 2, Agricultural soils (3C2+3C3+3C4+3C7) 3, Enteric fermentation (3A1) Waste 1, Agricultural waste burning (3C1b) 2, Solid waste incineration (4C) 3, Solid waste landfills (4A+4B)
² CEDS v_2021_04_21 CH ₄	1, Energy 2, Industrial 3, Solvents production and application	0, Agriculture 1, Transportation 2, Residential, commercial, other 6, Waste 7, International shipping
EDGAR v6.1 NO _x	1, Power industry (1A1a) 2, Refineries and transformation industry (1A1b+1A1ci+1A1cii+1A5biii+1B1b+1B2aiii6+1B2biii3+1B1c) 3, Combustion for manufacturing (1A2) 4, Fuel exploitation (1B1a+1B2aiii2+1B2aiii3+1B2bi+1B2bi i) 5, Chemistry process (2B) 6, Energy for building (1A4 +1A5) 7, Iron and steel production (2C2) 8, Fossil fuel fires (5B) 9, Non-ferrous metals production (2C3-C5) 10, Food and paper (2H)	Transportation 1, Aviation (1A3a) 2, Railways, pipelines, off-road transport (1A3c+1A3e) 3, Shipping (1A3d) Agricultural 1, Manure management (3A2) 2, Agricultural soils (3C2+3C3+3C4+3C7) Waste 1, Agricultural waste burning (3C1b) 2, Solid waste incineration (4C)

172

¹The codes in parentheses are based on IPCC 2006 used by EDGAR v7.0 to generate each sector.

173

²CEDS provides monthly sectoral methane emissions, in which the category is illustrated by the number.

174

175 2.3 Divergence calculation

176 The basic methodology has been described in Liu et al. (2021). Here, we have improved
177 the procedure to estimate CH₄ emissions from TROPOMI retrieved XCH₄ consisting
178 of three steps: (1) The use of daily MODIS/Aqua AOD 10 km L2 dataset (v6.1) and
179 daily CAMS gridded AOD re-analysis data to filter unreliable retrievals of TROPOMI
180 XCH₄. (2) Derive the enhancements of XCH₄ in the PBL (X_d^{PBL}) and non-divergent
181 winds from ERA5 wind dataset, which are then used to calculate the spatial divergence
182 and the preliminary methane emission. (3) Apply a posterior spatial correction to
183 subtract the contribution of the residue of the regional background, and identify
184 possible false sources by using a temporal filter.

185 Our method to estimate the preliminary methane emission E' over a certain period is
186 based on the divergence method described by Beirle et al. (2019) for NO_x emissions
187 and specifically for methane by Liu et al. (2021):

$$188 \quad E' = \overline{D_d^S} = \overline{\nabla \cdot (X_d^{PBL} - X_d^B) \times A_d^{PBL} \vec{w}} \quad (1)$$

189 where D_d^S is the daily divergence of a source. X_d^{PBL} is the daily XCH₄ in the Planetary
190 Boundary Layer (PBL) that is calculated by subtracting the vertical column of methane
191 above the PBL from the TROPOMI observations. [Estimating the XCH₄ in lower
192 atmosphere is quite important since the enhancement due to the transport in the upper
193 atmosphere is irrelevant to the ground emissions.](#) This vertical column above the PBL,
194 is based on the model results of EAC4 of CAMS [at a relative high spatial resolution,
195 0.75° horizontally and 60 layers vertically](#) (Inness et al., 2019), [with methane serving
196 as a background species for chemical reactions.](#) This EAC4 model run contains no *a*
197 *priori* CH₄ emissions. [Thus, the spatial distribution of CH₄ is mainly driven by
198 transport and orography, which will be subtracted from TROPOMI observations to
199 estimate the PBL concentration of CH₄. It is important to note that t](#)The total dry air
200 column from the EAC4 dataset is constrained by the TROPOMI retrieval for each pixel,
201 [which guarantees the mass conservation.](#) We fixed the PBLH at 500 meters above the
202 ground considering the PBLH from the reanalysis dataset has large uncertainties and is
203 occasionally too shallow (Guo et al., 2021). [The favorable height is suggested to be
204 500-700 meters above the ground considering the systematic difference between EAC4
205 dataset and TROPOMI observations \(Liu et al., 2021\).](#) X_d^B is the regional background
206 of X_d^{PBL} , which is defined as the average of the lower 10 percentile of its surrounding
207 ± 3 grid cells in the zonal direction and meridional direction ($7 \times 7 = 49$ grid cells in total
208 by taking the current grid cell as the center) considering the extensive variations of the
209 orography in the Middle East. The daily regional background is built when more than
210 10 grid cells have valid retrievals in this domain. A_d^{PBL} is the corresponding air density
211 column in the PBL. The details to derive X_d^{PBL} and A_d^{PBL} can be found in Liu et al.
212 (2021). The advantages of including X_d^B are (1) it can be used to diagnose the

213 contribution of inhomogeneous background, especially over mountains and coastal
 214 regions, and (2) the system biases between CAMS and TROPOMI, which leads to
 215 biased X_d^{PBL} , is included in both and can be greatly reduced by subtracting X_d^B from
 216 X_d^{PBL} .

217 The daily wind field (\bar{w}) halfway the height of the PBL (PBLH) close to the overpass
 218 time is obtained from the ECMWF. Wind speeds are constrained between 0 m/s to 10
 219 m/s because the divergence method works when advective transport takes place, and
 220 extremely high wind speed are unfavorable for a method based on the regional mass
 221 balance. Local wind-field changes induced by complicated orography inevitably leads
 222 to a certain pattern of wind divergence ($\overline{D_d^W}$), which further influence

$$223 \quad D_d^S = \bar{w} \nabla (XCH_4^{PBL} - XCH_4^B) + (XCH_4^{PBL} - XCH_4^B) \nabla \bar{w} \quad (2)$$

224 Liu et al. (2021) corrected E' by using an empirical correction by using a spatial
 225 correlation between $\overline{D_d^S}$ and $\overline{D_d^B}$ to account for the effect of inhomogeneous background
 226 and $\nabla \bar{w}$ over Texas, where the terrain is relatively flat and less affected by mountains.
 227 To better reduce the effect of winds, we followed the method ~~proposed~~imposed by Sims
 228 (2018) to iteratively remove the gradients of $\nabla \bar{w}$ on each day to get a non-divergent
 229 wind field, V component (south-north) and U component (west-east), for the calculation
 230 of Eq. (1). The positive values of $\overline{D_d^S}$ due to orography-raised wind near Tehran in Fig.
 231 2d are largely reduced (Fig. 2f) by using a non-divergent wind field. The magnitudes
 232 of $\overline{D_d^B}$ in Fig. 2e also get close to $\overline{D_d^S}$. Before we applied this change, we tested the non-
 233 divergent method in the GEOS-Chem simulation that was used in Liu et al., (2021). We
 234 found that this step slightly improved the capability of the method in resolving the
 235 spatial variability of sources (Figure S2), but underestimate the final emission by about
 236 15% in the GEOS-Chem simulation. In contrast, when deriving the emissions from
 237 TROPOMI, using a non-divergent wind field especially improves the robustness over
 238 coastal areas and typically increases emissions by 5-20% for most cases (Table S2
 239 shows an example). The difference in change of emissions between GEOS-Chem
 240 simulation and TROPOMI is primarily due to the correction of the final estimated
 241 emissions. As was mentioned in the manuscript, the final emission based on the
 242 divergence ($\overline{D_d^S}$). (Fig. 2d) apparently contains the residual of the divergence of
 243 background ($\overline{D_d^B}$) (Fig. 2c), which is highly correlated with wind divergence ($\overline{D_d^W}$).
 244 However, this dependence is much smaller for the GEOS-Chem simulation and for the
 245 emissions derived from TROPOMI by using non-divergent wind. The procedure and

246 the evaluation of removing the wind divergence from the original wind field are
 247 explained in Part B in SI. Generally, using a non-divergent wind field can improve the
 248 capability of the method in resolving the sources, both in a model simulation and in
 249 TROPOMI observations.~~the was in the mentioned above forfor~~
 250 ~~The procedure of~~
 251 ~~removing the wind divergence from the original wind field is explained in Part B in~~
SI simulation fors.

252 2.3 Estimating emissions based on the divergence

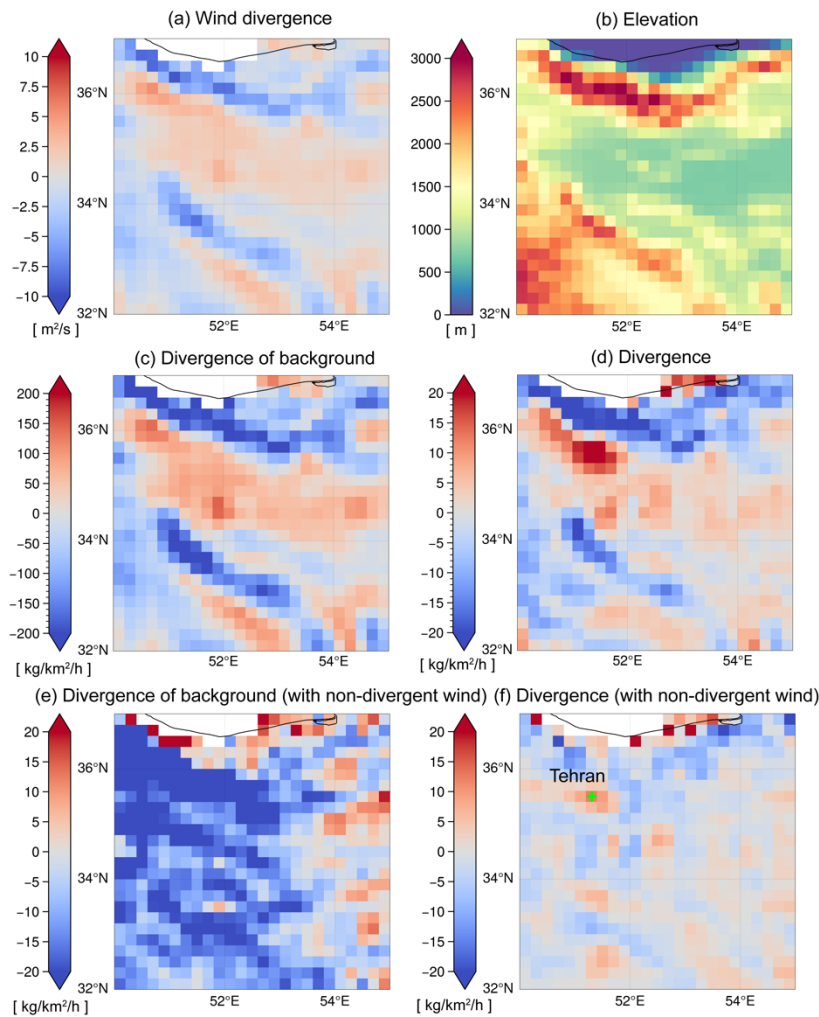
253 The inhomogeneous spatial distribution of $\overline{D_a^B}$ indicates the possible residue of the
 254 regional background we built in Sect. 2.2. Therefore, we evaluate the contribution from
 255 the residue background for each grid cell with positive E' by checking the spatial
 256 correlation between $\overline{D_a^B}$ and $\overline{D_a^S}$ in the domain that we defined to build the regional
 257 background (its surrounding ± 3 grid cell). For grid cells with positive E' , a linear
 258 regression is applied to its surrounding ± 3 cells:

$$259 \quad y_i = k \cdot x_i + b \quad (3)$$

260 where y_i stands for $\overline{D_a^S}$ and x_i stands for $\overline{D_a^B}$ of grid i . k and b are the slope and intercept
 261 of the linear regression, respectively. If Eq. (3) is applicable to the center grid, it implies
 262 the residue of the background still contributes to E' and should be subtracted. This
 263 linear correlation can be distinctive over locations with large variations in orography
 264 (e.g., mountains, coastal areas). If more than 68% of the grid cells and the grid cell itself
 265 fall within the prediction lines of Eq. (3), estimated emissions are set to zero because
 266 $\overline{D_a^S}$ can be fully predicted by $\overline{D_a^B}$ according to Eq. (3). The grid cells are considered to
 267 be influenced by residue background only when Eq. (3) is significant (p-value < 0.01),
 268 and they are further corrected by the spatial correction:

$$269 \quad E^{corr} = E' - (k \cdot \overline{D_a^B} + b) \quad (4)$$

270 in which $(k \cdot \overline{D_a^B} + b)$ is regarded as the contribution from the remaining background,
 271 which should be subtracted from the preliminary estimated emissions, E' . In addition,
 272 we find that areas with negative E' together with negative $\overline{D_a^B}$, implying no significant
 273 sources exist. The final estimated emissions at grid cells with negative E' are also set
 274 to zero (Liu et al., 2021).



276 **Figure 2.** (a) The spatial distribution of original wind divergence ($\overline{D_d^W}$). (b) Elevation
 277 map generated from the GMTED2010 data set at 30 arcsecs
 278 (http://topotools.cr.usgs.gov/GMTED_viewer/). (c) Divergence of the background ($\overline{D_d^B}$)
 279 calculated with original daily wind field in 2019. (d) Divergence of methane
 280 enhancement ($\overline{D_d^B}$) under 500 meters with original daily wind field. (e)-(f) are similar
 281 to (c)-(d) but with the daily non-divergent wind field (U and V). The green “+” in (f)
 282 is used to generate the time series of D_d^B and D_d^S in Figure 5b.

283

284 2.4 Build temporal filter to identify possible false sources

285 The artifacts caused by the variability of spectral albedo (e.g., specific soil types and
 286 interferences in the spectral range of the retrieval windows) have been generally

287 reduced in the WFMD v18 product (Schneising et al., 2023). The unrealistic
 288 enhancements are reduced/removed over most locations. However, the biases
 289 mentioned above can still exist in some places, as shown in Figure 3. In the northeast
 290 near Riyadh, the stripe-shaped XCH₄ enhancements (Fig. 3a) coincide with the
 291 locations of high albedos (Fig. 3b) that cannot be explained by the changes of elevations
 292 from southwest to northeast (Fig. 3c). The relevant correction has been done by
 293 machine learning calibration in the WFMD v18 product, thus we found no universal
 294 pattern that can be used to describe the relationship among XCH₄, surface albedo and
 295 aerosol. Therefore, we do not correct this kind of bias, following Liu et al. (2021), to
 296 avoid double-correction. Alternatively, we try to find an objective way to filter false
 297 emissions caused by retrieval artifacts.

298 A grid cell with a large E' but no significant linear correlation between $\overline{D_d^S}$ and $\overline{D_d^B}$
 299 contains either a source or ~~is~~ caused by artifacts in the retrieval, such as the case shown
 300 in Fig. 3. If the enhancement is a kind of artifact; for example, caused by a bright surface,
 301 it behaves more like a constant over days. Therefore, temporal variations of D_d^S will be
 302 mainly dominated by daily variations of the background, according to Eq (1).
 303 Considering that the values of D_d^B are much higher than D_d^S , as XCH_4^{PBL} is used to
 304 calculate D_d^B while $(XCH_4^{PBL} - XCH_4^B)$ is used to calculate D_d^S , we normalize time
 305 series of D_d^S and D_d^B , respectively. This normalization allows for a better comparison of
 306 their temporal variations (amplitudes). The temporal filter is based on their normalized
 307 time series and built as follows. Firstly, we remove the grid cells that have less than 10-
 308 day records. Next, if more than half of the days in the time series of a grid cell have a
 309 normalized positive D_d^S larger than D_d^B , the derived source (grid cell) is considered to
 310 ~~be a real source and not an retrieval artifact. have high confidence level.~~ As an example,
 311 we take a grid cell (showing with a green “+” in Fig. 3e) that is affected by the albedo
 312 near Riyadh. It has a larger $\overline{D_d^S}$ than its surrounding grid cells, but the linear regression
 313 is not applicable here (p_value of Eq. (3) is 0.2), suggesting the regional background
 314 we built is not biased. However, only 20% (value of R in Fig. 4) of the total reliable
 315 days in 2019 have larger positive normalized D_d^S (Fig. 4b), indicating the daily variation
 316 is not significantly different from its background. Hence the reliability of this source
 317 needs to be checked. In contrast, more than 50% of the total days of the grid cell, which
 318 is verified as a true source in Tehran (a green “+” in Fig. 3e), have larger positive
 319 normalized D_d^S . In this way, the emissions from an artifact or random noise from the
 320 retrieval can be objectively identified. In this study, we set the temporal filter such that
 321 at least more than 50% observations from the time series have a larger positive
 322 normalized D_d^S than the normalized D_d^B .

323 However, we should also be aware that the threshold of the temporal filter used in this
 324 study is relatively rigid, possibly excluding sources that occasionally release a large
 325 amount of methane, like intermittent oil/gas leakage and inappropriately burned waste

326 gases. The preserved sources that pass the temporal filter are suggested to be more
327 constant ~~than that possible did but not passed the temporal filter~~. For grid cells not
328 affected by retrieval issues, the role of the temporal filter is more like an indication of
329 the persistence or regional significance of a source, and the emissions without the
330 temporal filter might, in some cases, be more realistic. The role of the temporal filter
331 will be further discussed in Sect. 3

332 The divergence method requires sufficient temporal records (typically more than 7 days
333 with valid observation for a grid cell) to derive robust results. Thus, the divergence on
334 a single day does not provide a realistic emission for that day, and taking the standard
335 deviations for individual days does not reflect the uncertainty or variability of a source.
336 In addition, this method is not suitable for sources with a few intermittent releases, such
337 as sudden leaks in oil and gas production. $\overline{D_d^S}$ can be a quite large positive value for this
338 kind of source. However, a small number of large releases in a time series may lead to
339 a removal of this source by the temporal filter (see the case of Fig. 6 in Sect. 4), which
340 is built for automatically detecting retrieval artifacts over a large domain. In order to
341 keep as many real sources as possible, we apply a Monte Carlo experiment to each
342 possible source to estimate the uncertainty of the derived emissions and to evaluate the
343 robustness/reliability of a source. The procedure is as follows:

344 ~~In addition, we use a Monte Carlo experiment to assess the uncertainty of the emissions.~~
345 ~~We randomly select 80% of the time series of D_d^S of a grid cell and calculated emissions~~
346 ~~based on this subset. The one standard deviation of those subsets will be used as an~~
347 ~~estimation of the uncertainty of the emission of this grid cell. The details of building~~
348 ~~the temporal filter and calculating the uncertainties are explained in SI part C.~~

- 349 (1) We randomly choose 80% of the sampling days from a time series in a year as a
350 subset. We derive a new emission, E_i , and count the ratio, R_i , of the number of days
351 that have larger normalized D_d^S than normalized D_d^B .
- 352 (2) Repeat step (1) 30 times for a time series that has more than 20 sampling days while
353 10 times for the one that have fewer days to derive the set of emissions, $\{E_i\}$, and
354 the set of ratios, $\{R_i\}$ for each possible source. R_i is used as the temporal filter in
355 each subset.
- 356 (3) Take one-standard deviation of the set $\{E_i\}$ as an uncertainty of a source. If the
357 median value (R) of $\{R_i\}$ is greater than 0.5, this source is regarded having high
358 confidence, which means these emissions are constantly released and likely not
359 caused by a retrieval artifact.

We also investigate the choice of the percentage of the time series and the number of the iterations. 80-70% percent can be a reasonable range that ensure the representativeness as well as randomness of sampling days. We have tested the number of iterations from 10 to 50 times. The uncertainty map such as Fig. 5c become stable after 20 iterations, and 30 iterations can ensure the robustness as well as the efficiency of the calculation.

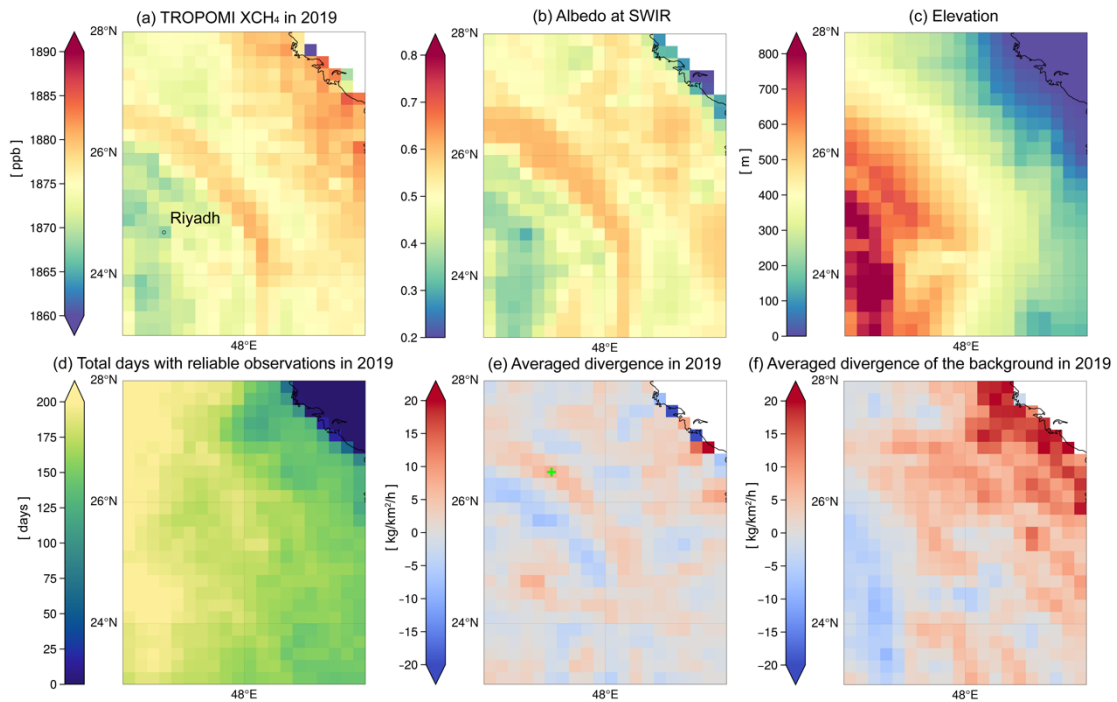
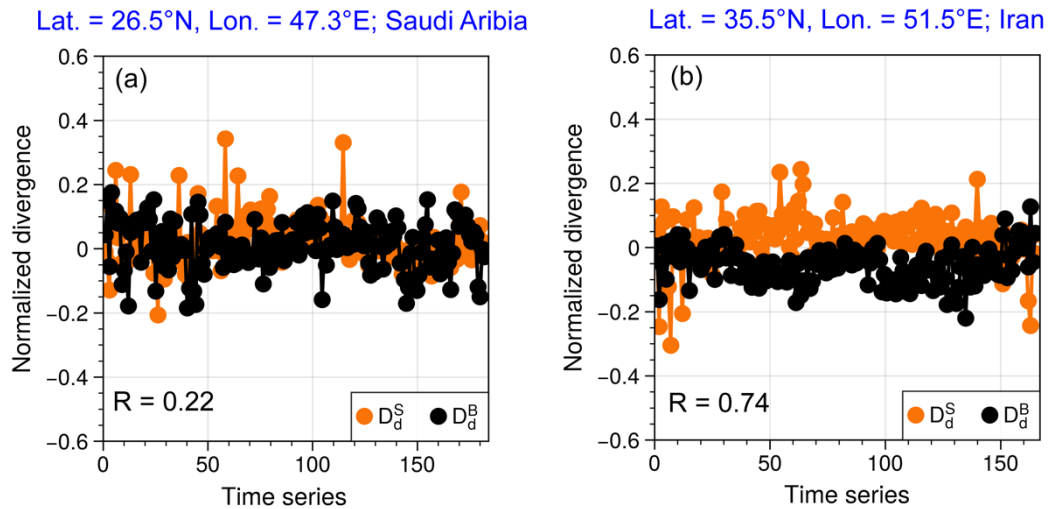


Figure 3. Gridded $0.2^\circ \times 0.2^\circ$ annual average of (a) TROPOMI observed XCH_4 and corresponding (b) TROPOMI apparent albedo at the short-wave infrared wavelength (SWIR). (c) The gridded elevation map that is generated from the GMTED2010 data set at 30 arcsec (http://topotools.cr.usgs.gov/GMTED_viewer/). (d) The total number of valid observation days in 2019. (e) Averaged daily divergence ($\overline{D_d^B}$) and (f) divergence of the background ($\overline{D_d^S}$) in 2019. The green “+” in (e) is used to generate the time series of D_d^B and D_d^S in Figure 4(a).



375 **Figure 4.** The time series of normalized D_d^S (orange line) and D_d^B (black line) of the
 376 grid cell in (a) Saudi Arabia and (b) Iran. The “R” in the lower left corner stands for the
 377 ratio of the number of days with a larger positive normalized $\overline{D_d^S}$ than $\overline{D_d^B}$ related to the
 378 total number of sampled days.

379

380 **3 Results**

381 *3.1 Deriving the final emissions with the temporal filter*

382 After we derived emissions based on the divergence, the possible false sources are
 383 further identified by the temporal filter. The strict temporal filter is introduced to
 384 objectively exclude artifacts related to retrieval issues. However, to a grid cell that is
 385 not affected by retrieval issues, the temporal filter acts more like an indication of the
 386 persistence of a source. Namely, methane is intermittently released from this source.
 387 Here we selected two areas in the Middle East to illustrate the role of the temporal filter
 388 in the emission estimation. Our methane annual emissions are then compared with three
 389 widely-used methane emission inventories in the same year, 2019. Other auxiliary
 390 datasets such as NO_x emission inventories, methane plume complexes detected by
 391 EMIT imaging spectrometer and heating sources identified by VIIRS are also used to
 392 better evaluate our derived emissions.

393 Figure 5a and c show all possible sources and their relative uncertainties, respectively.
 394 Fig. 5b shows the final emissions after excluding the grid cells with emissions less than
 395 3 kg/km²/h, which is used as detection threshold of a source in this study. It is estimated
 396 by using the detection threshold of TROPOMI XCH₄ (Hu et al., 2018, [Schneising et al.,](#)
 397 [2023](#)) and the approach in [Jacob et al., \(2022\)](#). The detection threshold of methane
 398 source from TROPOMI is depending on many factors such as source types, inversion

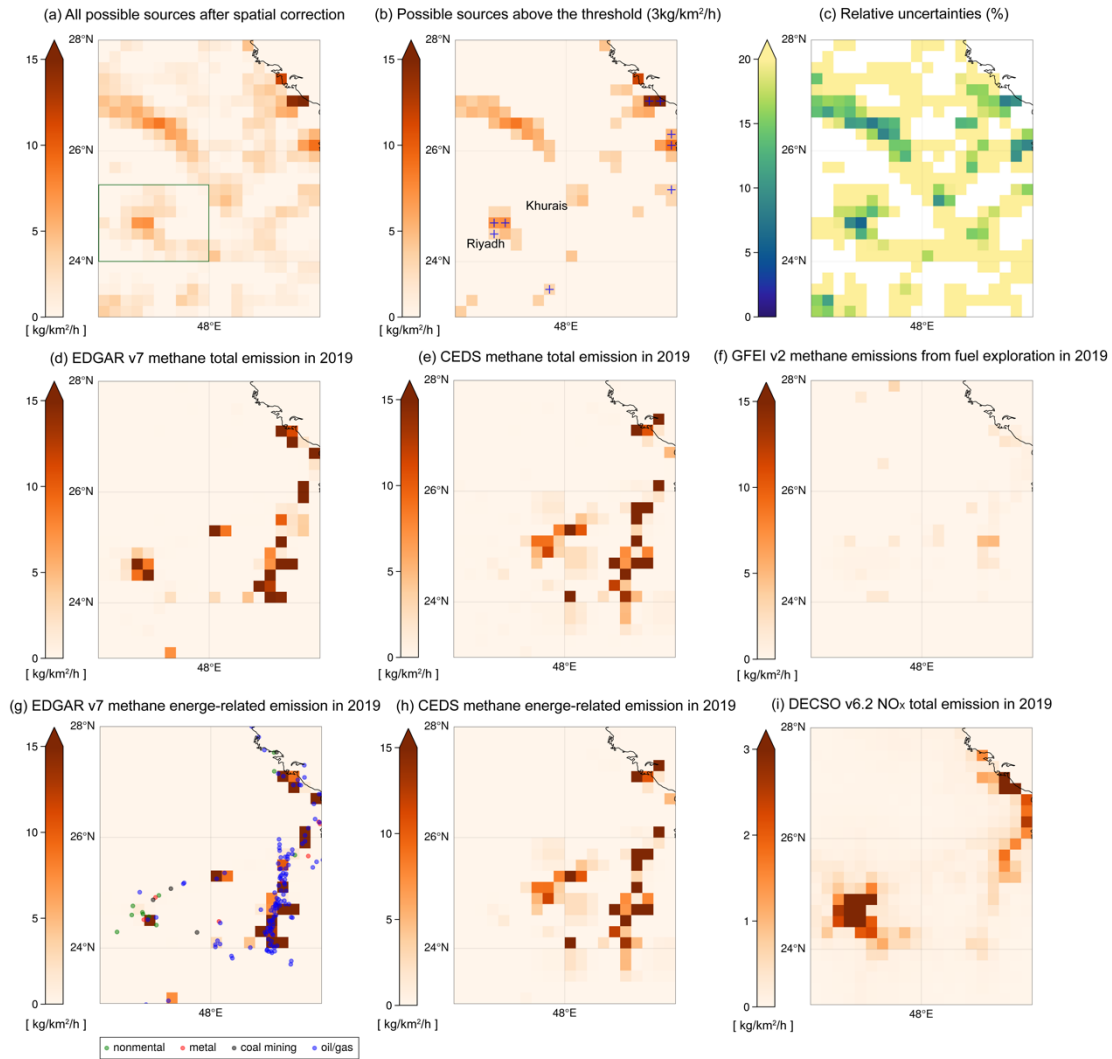
399 methods and temporal coverage over a location etc., which can vary from ~ 0.5 kg/km²/h
400 to 12.5 kg/km²/h (Lauvaux et al., 2022; Dubey et al., 2023; Jacob et al., 2016; 2022).
401 Fig. 5a suggests presence of small sources around the center of Riyadh, where a number
402 of heating sources are detected by VIIRS. Additionally, small sources are detected in
403 the south to Riyadh, where dairy farms and industry areas are located. The spatial
404 distributions over two areas are similar to the DECSO NO_x emissions, indicating
405 existence of human activities. However, we found that sources below the detection
406 threshold show large uncertainties (>20%) in this study, which means the method is not
407 robust to distinguish these small sources from the regional background.

408 Both constant sources and artifacts (the “stripe” in the north of Riyadh) show small
409 relative uncertainties (Fig.5c) due to continuous regional enhancement of XCH₄. Only
410 a few sources pass the temporal filter in the middle of Saudi Arabia (marked by blue
411 “+” in Fig. 5b, indicating they are with high confidence). However, some facilities are
412 found over the Khurais oil field in Google Earth image while it fails to pass the temporal,
413 indicating they might be true but not constant. Another similar case is in the middle of
414 the Syria Arab Republic, where many methane plumes along the Euphrates River are
415 detected by the EMIT instrument (Fig. 6b) but reported quite low by three bottom-up
416 emission inventories. They are reported as non-continuous sources (fail to pass the
417 temporal filter) in our emission inventory (Fig. 6a). Thus, applying the strict temporal
418 filter in an area without retrieval issues is aim at identifying continuous sources. In
419 addition, except for the capital, Riyadh, both EDGAR and CEDS show that the primary
420 type of sources in Saudi Arabia is energy related. The locations of oil/gas-related fires
421 also match well with the sources of methane in the eastern area in Fig. 5g. However,
422 our estimates (Fig. 5b) and methane emissions from the fuel exploitation reported by
423 GFEI v2 (Fig. 5f) are quite low (lower than the TROPOMI detection threshold) in the
424 eastern oil/gas production area. This finding is similar to the result of Lauvaux et al.
425 (2022) that fewer ultra-emitters of methane are detected by using the TROPOMI CH₄
426 operational product (Lorente et al., 2021) in Middle Eastern countries such as Kuwait
427 and Saudi Arabia, which could be attributed to fewer accidental releases and/or
428 stringent maintenance operations. Using the locations and frequency of flares to
429 estimate the methane emission in bottom-up emission inventories could have led to
430 overestimation of the methane emissions in this region.

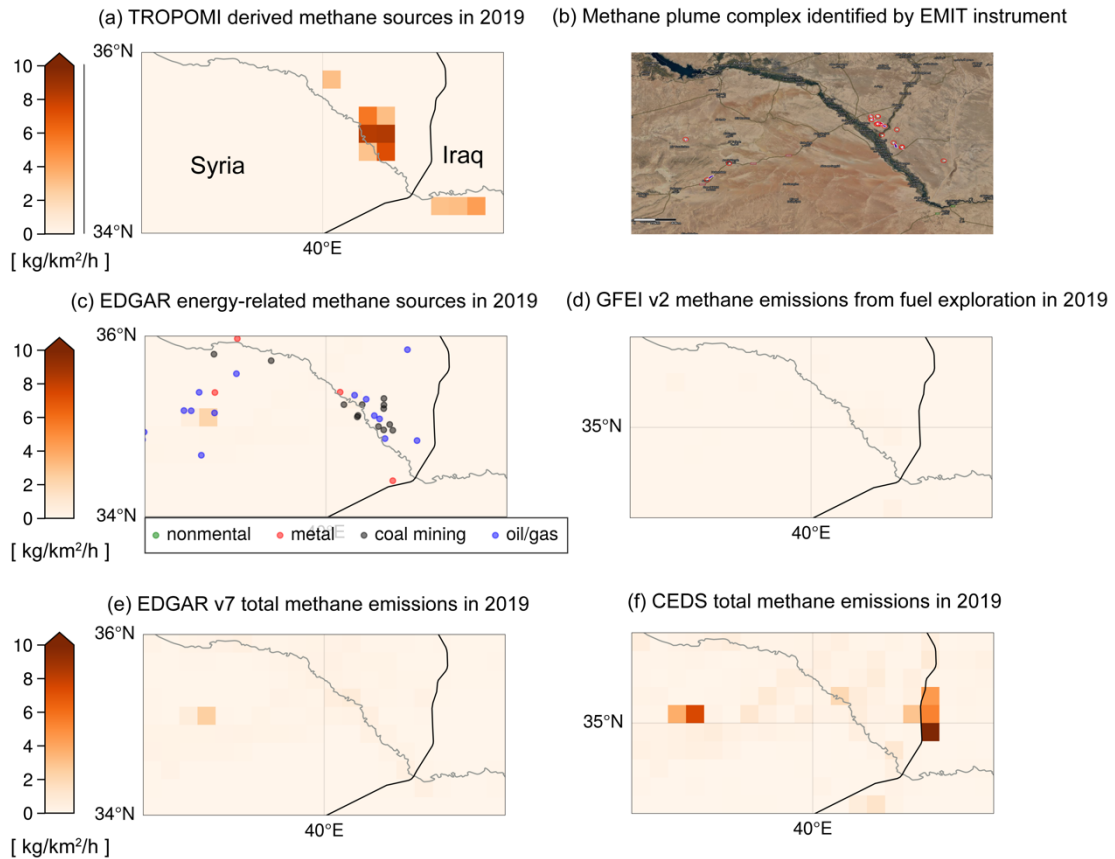
431 In contrast, Figure 7 show the case over Tehran and its surroundings. Most sources in
432 this area pass the strict temporal filter, indicating they are quite constant. Five areas are
433 identified as hotspots of methane sources in Fig. 7b. Fig. 7d-f shows the spatial
434 distributions of methane sources estimated by EDGAR, CEDS and GFEI in 2019. The
435 bottom-up emission inventories show lower methane emissions than our results. The
436 dominant category of methane sources in this area is not energy-related but others like
437 waste treatment and agriculture (see classification in Table-1), as suggested by EDGAR
438 and CEDS. A number of heat sources due to mental or non-mental industry production
439 are also identified by VIIRS over these hotspots. A good match in locations between

440 methane and NO_x sources over Tehran, Isfahan, and Atarabad is found when we further
441 examine NO_x source distributions in EDGAR and DECSO. One possible reason for the
442 consistence over these areas can be that the methane emissions may come from waste
443 treatment in cities, where landfilling is the most common way of municipal solid waste
444 (MSW) disposal in Iran (Pazoki et al., 2015). Fig. 7c presents a case of methane plume
445 identified by EMIT instrument on 23th April 2023 near Kashan power plant that is
446 apparently not reported in current inventories. Actually, some facilities have been found
447 in Google Earth images near Kashan, which are also identified by our method in Fig.
448 7b. Another hotspot area located between Tehran and Kashan is ~~the area~~ near Kavir
449 National Park, where we currently have no clear explanations ~~for the about~~ emissions.

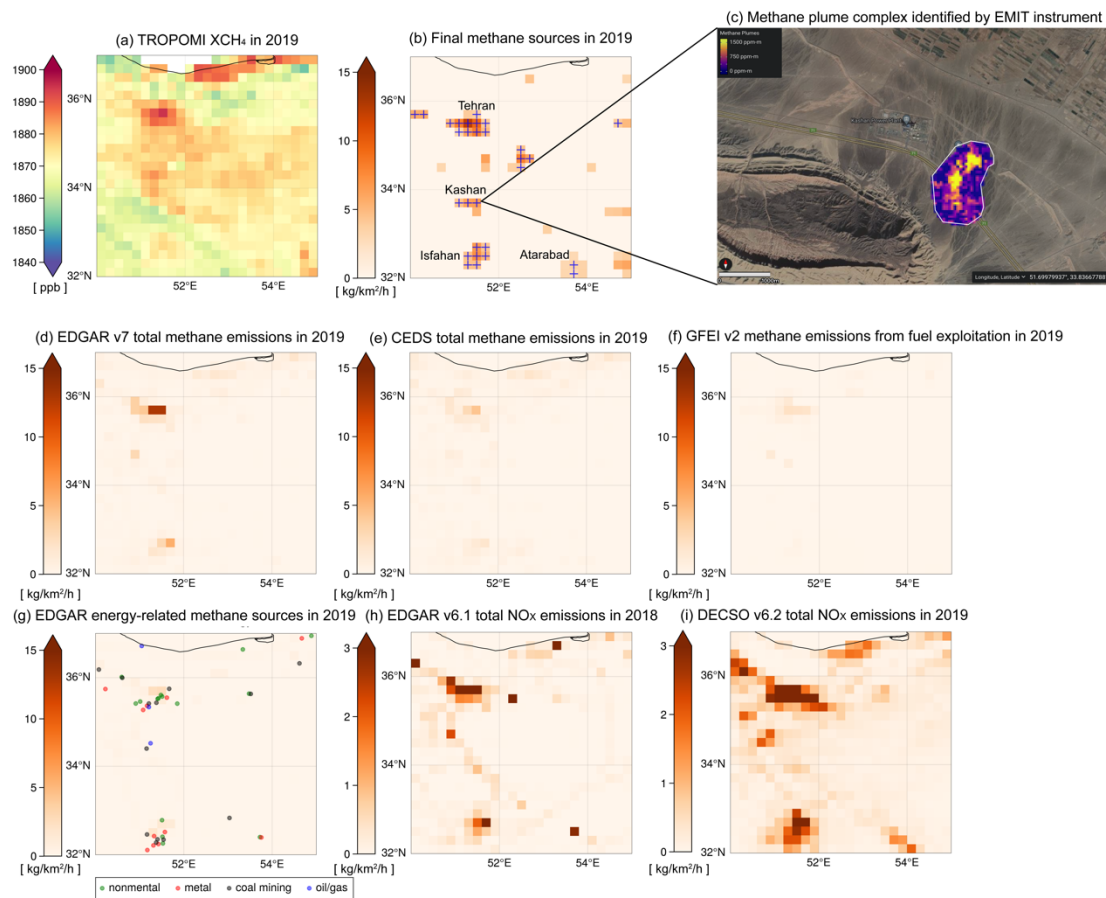
450



451 **Figure 5.** (a) Averaged annual methane ~~total~~ emissions derived from the divergence
 452 after the spatial correction in the middle of Saudi Arabia. (b) All possible sources above
 453 the ~~TROPOMI~~ detection threshold of emissions in this study ($3\text{kg}/\text{km}^2/\text{h}$). Grid cells
 454 that pass the temporal filter are marked by blue “+”. (c) The relative uncertainty of
 455 derived methane emissions in (a). (d) EDGAR v7.0 averaged annual methane total
 456 emission in 2019. (e) CEDS v_2021_04_21 averaged annual total methane emissions
 457 in 2019. (f) GFEI v2 averaged annual methane emissions from fuel exploration in 2019.
 458 (g) Energy-related methane emissions from EDGAR v7.0 overlapped with the
 459 industrial heat sources identified by VIIRS instrument. (h) CEDS v_2021_04_21
 460 energy-related methane emissions in 2019. (i) Averaged annual DECSO v6.2 NO_x total
 461 emission in 2019. The spatial resolution of all emission data showing here is $0.2^\circ \times$
 462 0.2° .



463 **Figure 6.** (a) Averaged annual methane emissions over Syria from TROPOMI
 464 observations in 2019. (b) The detected methane plume complex (red circles) by the
 465 EMIT instrument. (Note: EMIT was launched in 2020 and methane plumes are recorded
 466 since 10th August 2022; Source: [https://earth.jpl.nasa.gov/emit/data/data-](https://earth.jpl.nasa.gov/emit/data/data-portal/Greenhouse-Gases/)
 467 portal/Greenhouse-Gases/) (c) Energy-related methane emissions from EDGAR v7.0
 468 overlapped with the industrial heat sources identified by the VIIRS instrument. (d)
 469 GFEI v2 methane emissions from the fuel exploitation in 2019. (e) EDGAR v7.0
 470 emission inventory in 2019. (f) CEDS v_2021_04_21 total methane emissions in 2019.
 471 The spatial resolution of all emission data showing here is $0.2^\circ \times 0.2^\circ$.



473 **Figure 7.** (a) The spatial distribution of TROPOMI observed XCH₄ in 2019 on a grid
 474 of 0.2°. (b) The methane sources derived from TROPOMI after the spatial correction
 475 and are higher than 3kg/km²/h (inferred from the detection threshold of TROPOMI
 476 XCH₄). The grid cells with high confidence, passing the temporal filter, are marked by
 477 a blue "+". (c) The detected methane plume complex by [the EMIT instrument](https://earth.jpl.nasa.gov/emit-mmgis-lb/?s=e7z1z)
 478 on 23th April 2023 (Source: <https://earth.jpl.nasa.gov/emit-mmgis-lb/?s=e7z1z>). [EMIT](https://earth.jpl.nasa.gov/emit-mmgis-lb/?s=e7z1z)
 479 [was launched in 2020 and methane plumes are recorded since 10th August 2022.](https://earth.jpl.nasa.gov/emit-mmgis-lb/?s=e7z1z) (d)
 480 EDGAR v7.0 averaged annual methane total emission in 2019. (e) CEDS
 481 v_2021_04_21 averaged annual total methane emissions in 2019. (f) GFEI v2 averaged
 482 annual methane emissions from the fuel exploitation in 2019. (g) Energy-related
 483 methane emissions from EDGAR v7.0 overlapped with the industrial heat sources
 484 identified by [the VIIRS instrument](https://earth.jpl.nasa.gov/emit-mmgis-lb/?s=e7z1z). (h) Averaged annual EDGAR v6.1 NO_x total
 485 emission in 2019. (i) Averaged annual DECSO v6.2 NO_x total emission in 2019.

486 3.2 Annual CH₄ emissions over the Middle East based on TROPOMI

487 In Figure 8, we select five hotspot regions in the Middle East [hardly influenced by](https://earth.jpl.nasa.gov/emit-mmgis-lb/?s=e7z1z)
 488 [retrieval issues](https://earth.jpl.nasa.gov/emit-mmgis-lb/?s=e7z1z) to further assess the annual regional emissions— [from 2019 to 2022.](https://earth.jpl.nasa.gov/emit-mmgis-lb/?s=e7z1z)
 489 [Before we calculate the emissions of each region, we checked spatial patterns of XCH₄](https://earth.jpl.nasa.gov/emit-mmgis-lb/?s=e7z1z)
 490 [and albedo from TROPOMI, as well as land features, to ensure no suspicious retrieval](https://earth.jpl.nasa.gov/emit-mmgis-lb/?s=e7z1z)

491 [artifact is included as a source. The emissions are based on all possible sources and](#)
492 [only confident sources are shown.](#) ~~Therefore,~~ the results of all possible sources (pink
493 bars) may be more representative of the total emissions in these areas, and the emissions
494 passing the temporal filters (blue bars) can be used to estimate the contribution of
495 constant sources. [Here we should clarify that the constant source in our paper does not](#)
496 [refer to one with a constant emission factor but indicates a source that continually](#)
497 [releases methane for most days of a year.](#) The areas used to calculate annual emissions
498 (bars in Fig. 8) are shown as dark green rectangles in the insets on the top. The emission
499 map in each panel of Fig. 8 is the annual methane emissions of EDGAR v7.0 in 2019.
500 The energy-related sectors and the other categories (waste, agriculture, and
501 transportation) of EDGAR v7.0 methane emissions from 2018 to 2021 are displayed by
502 the first stacked green/yellow bars in Fig. 8a–e. The category-based annual emissions
503 of CEDS in 2018 and 2019 are shown in the last stacked purple/orange bars. The
504 estimate of GFEI for the fuel exploration in 2019 is shown as a red asterisk overlapped
505 on the third column. We should clarify that our estimate for the total emission in each
506 year is the sum of sources that are higher than 3kg/km²/h in the study area, but the total
507 emission reported by a bottom-up emission inventory includes grid cells with emissions
508 across all ranges. Thus, theoretically our estimates will underestimate the real emissions.

509 The main type of methane sources in Tehran and Isfahan given by EDGAR and CEDS
510 is waste, and the energy-related sources are not oil/gas production based on VIIRS
511 detected fire types and EDGAR’s prediction (Fig. 7g). The derived methane emissions
512 are also more constant. Smaller differences are found between the blue and pink bars
513 than Riyadh, West of Turkmenistan and Iran & Iraq (Fig. 8c-e). Our estimates in Tehran
514 are 12-30% higher and 33-52% higher than EDGAR’s and CEDS’s estimates for
515 constant sources, respectively. [Our result \(220 kt/yr for 2018-2021\) is much lower than](#)
516 [the emission estimated by de Foy et al., \(2023\) \(953 kt/yr for 2017-2021\) over Tehran,](#)
517 [which is 8.3 times higher than EDGAR v6.0’s estimates \(114 kt/yr\) used in that paper.](#)
518 [The possible reasons could be different assumptions of the regional background and the](#)
519 [methods to calculate the emission of the area. The Gaussian model used by de Foy et](#)
520 [al., \(2023\) treated an urban area as one large source and integrated the emissions along](#)
521 [the “plume”, whereas our total emission for a certain area is the sum of individual](#)
522 [sources that are derived from the divergence method.](#) GEFI’s estimate for the fuel
523 exploration is 2-3 times higher than EDGAR’s and CEDS’s estimates, indicating
524 possible underestimations of the two inventories in Tehran. The sources in Isfahan,
525 another Iranian metropolis, are also constant over time (very small difference between
526 blue and pink bars). However, our derived emissions are about 3 times higher than the
527 two inventories. Sources in our inventory are distributed over a wider area in Isfahan,
528 and their spatial distributions are similar to NO_x sources of EDGAR and DECSO,
529 indicating the emissions are very likely from activities in the city. Although Isfahan has
530 been attempting to gradually transform the landfill-based disposal system into a modern
531 system with less production of greenhouse gases, the high methane emissions we
532 derived might also imply that waste management is still a challenge (Abdoli et al.,

533 2016). A similar result was found by Chen et al. (2023), in which they found waste
534 emissions could be underestimated by more than 50% in certain Middle Eastern
535 countries like Iran, Iraq, and Saudi Arabia.

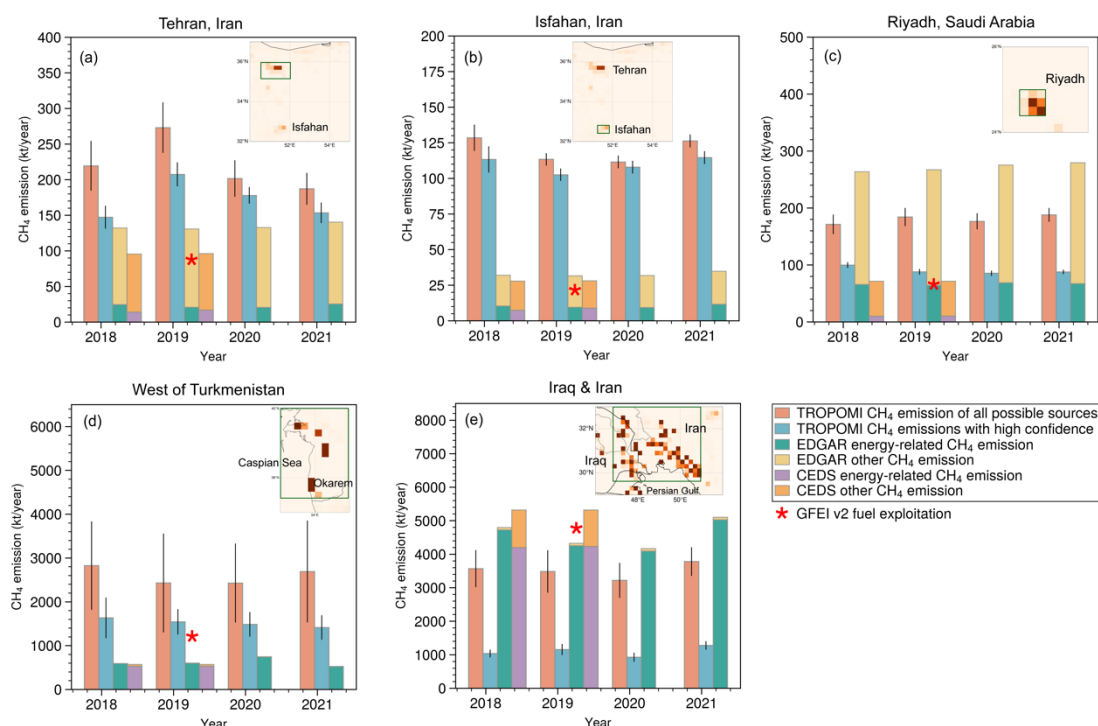
536 The total constant emissions we derived for Riyadh are half that of EDGAR but close
537 to CEDS's estimate. As shown in Fig. 5, the spatial distributions of various inventories
538 can be very different. The domain we used to calculate the total emission is defined by
539 the spatial distribution of EDGAR, but oil/gas-related flares are located in the northeast
540 of Riyadh (blue dots in Fig. 5g). However, including these cells only increases total
541 emissions by 5–8% because they are smaller than $3\text{ kg/km}^2/\text{h}$ therefore below the
542 detection threshold of TROPOMI. Moreover, ~50% of the emissions in Riyadh are
543 constant (have constant emission factor), which can be another reason of the large
544 discrepancy between different inventories.

545 Western Turkmenistan near the Caspian Sea and the coastal regions of Iran and Iraq are
546 two well-known oil/gas production areas in the Middle East. The energy-related sectors
547 (green bars) contribute more than 92% in the two regions based on EDGAR estimates.
548 The constant emissions derived from TROPOMI (blue bars) in the west of
549 Turkmenistan are quite comparable to GFEI's estimate but nearly two times higher than
550 estimates of EDGAR and CEDS. Although total methane emissions estimated by
551 EDGAR and CEDS are very similar, the spatial distributions of sources are different
552 (Figure S31). The constant sources of oil/gas there contribute to ~55% of the total
553 emissions over the four years based on our estimates, which agrees with Varon et al.
554 (2021), who concluded the sources here are intermittent, and the persistence rate is
555 ~40%. Our estimates will be four times higher than the total emissions of these two
556 inventories if all possible sources are included. The large uncertainty also implies that
557 resolving the sources here can be quite difficult because of the few observations near
558 the coast and the variabilities of the sources.

559 The annual variations in the coastal area of Iraq and Iran are consistent in EDGAR's
560 and our estimates (the offshore emissions in bottom-up emission inventories are
561 ignored because the observation of TROPOMI over ocean can be quite difficult). It
562 increased to surpass the total emission of 2018 in 2021 after a modest decline from
563 2018 to 2020. The fraction of constant sources is much less than in Western
564 Turkmenistan. Our estimates are comparable to EDGAR if all possible sources are
565 included. However, the total emissions from constant sources are quite low, and they
566 are comparable to the other methane emissions estimated by CEDS, which mainly come
567 from waste and are quite low in EDGAR estimates. Chen et al. (2023) found that oil/gas
568 emission derived from their inverse modeling with the TROPOMI observation is 43%
569 and 58% lower than in their bottom-up emission inventory over Iran and Iraq,
570 respectively. Lauvaux et al. (2022) also showed fewer ultra-emitters of methane are
571 detected by using the TROPOMI CH₄ operational product (Lorente et al., 2021) in
572 Middle Eastern countries such as Kuwait and Saudi Arabia, which could be attributed

573 to fewer accidental releases and/or stringent maintenance operations. Thus, for an area
 574 with many occasionally released methane, using a constant emission factor or flaring
 575 data as an index may lead to an overestimation of methane leakage from the oil/gas
 576 industry. In addition, we checked plume complexes detected by EMIT, and find that the
 577 max value of each plume complex can differ by an order of magnitude, implying the
 578 large variabilities of released methane here. The coarse spatial resolution of our
 579 emission data may smooth plume complexes and can be another reason of predicted
 580 lower emissions.

581



582 **Figure 8.** Regional total methane annual emissions estimated by EDGAR v7.0 and
 583 TROPOMI from 2018 to 2021. The areas used to generate bars in (a–e) are shown in
 584 dark green rectangles in embraced emission maps of total emissions of EDGAR in 2019.
 585 The ranges in latitudes and longitudes can be found in Table S1 in SI. A green bar
 586 represents the energy-related emissions, and a yellow bar represents the remaining
 587 methane emissions in EDGAR v7.0. A purple bar represents the energy-related
 588 emissions, and an orange bar represents the remaining methane emissions in CEDS
 589 v_2021_04_21. The blue bar is the total emission of sources that pass the temporal filter
 590 and are higher than 3kg/km²/h. The pink bar represents the total emission of all possible
 591 sources that are higher than 3kg/km²/h. All the emissions over water (the Caspian Sea
 592 and the Persian Gulf) are ignored because of too few observations and large
 593 uncertainties. An error bar represents the sum of uncertainties associated with each
 594 source in this area. The calculation of the uncertainty of a source (grid cell) is presented
 595 in Sect. 2.4 and the SI Part C.

596

597 **4 Conclusions**

698 An improved divergence method using non-divergent wind fields with ~~a~~the temporal
599 filter has been developed to better estimate CH₄ emissions from observations of the
600 TROPOMI instrument over areas with complicated orography and/or high albedo, like
601 the Middle East. The non-divergent wind largely reduces the biases caused by drastic
602 topography changes. The residue of the background (e.g., sources in Tehran, located in
603 a valley) is further subtracted from the emission through spatial correction. The
604 temporal filter is built to further exclude false sources due to retrieval issues. It also can
605 be used to test the persistency of sources over an area free of artifacts. We found that
606 emissions from wastes (e.g., landfills, wastewater) or agriculture (e.g., livestock farms)
607 can be quite persistent in time compared to the oil/gas-related sources in the Middle
608 East.

609 We further compared our annual regional total emissions with EDGAR v7.0, CEDS
610 v2021_04_21 and GFEI v2 for various regions in the Middle East with different source
611 categories from 2018 to 2021. The oil/gas productions at the coast of Iran and Iraq are
612 quite intermittent compared to the west of Turkmenistan where our estimate for
613 constant sources is quite comparable to the emission from the fuel exploitation
614 estimated by GFEI v2. The continuous release of methane from waste or farms can
615 contribute considerably to the total methane emissions in several metropolises in the
616 Middle East, which can be two times higher than EDGAR's and CEDS's estimates.

617 In future work, the role of the temporal filter can be largely reduced with new improved
618 retrieval products of TROPOMI CH₄. This will especially allow better estimates of
619 intermittent methane emissions.

620 *Acknowledgments*

621 *Competing interests.*

622 The authors declare that they have no competing interests.

623 *Funding.*

624 ESA project IMPALA, grant number: 4000139771/22/I-DT-bgh

625 ***Author contributions.***

626 ML, RVA, and MVW designed the experiment and analyze the results. ML performed
627 all calculations and visualized the results. The codes for estimating methane emissions
628 are mainly developed by ML and are supported by LB, HE and PV. HK and JD help to
629 visualize the results. The wind fields are extracted by HE. YL provides the category-
630 related VIIRS data. All co-authors contributed to review the manuscript.

631 ***Data and materials availability:***

632 TROPOMI/WFMD v1.8 methane Level-2 dataset is available at: [https://www.iup.uni-](https://www.iup.uni-bremen.de/carbon_ghg/products/tropomi_wfmd/)
633 [bremen.de/carbon_ghg/products/tropomi_wfmd/](https://www.iup.uni-bremen.de/carbon_ghg/products/tropomi_wfmd/)

634 EAC4 of CAMS, which used to be estimated the column above the PBL can be accessed
635 at: [https://ads.atmosphere.copernicus.eu/cdsapp#!/dataset/cams-global-reanalysis-](https://ads.atmosphere.copernicus.eu/cdsapp#!/dataset/cams-global-reanalysis-eac4?tab=overview)
636 [eac4?tab=overview](https://ads.atmosphere.copernicus.eu/cdsapp#!/dataset/cams-global-reanalysis-eac4?tab=overview)

637 EDGAR v7.0 for methane anthropogenic emissions and EDGAR v6.1 for NO_x
638 anthropogenic emissions are available at:
639 https://edgar.jrc.ec.europa.eu/overview.php?v=432_GHG

640 CEDS v_2021_04_21 for methane anthropogenic emissions is available at:
641 <https://data.pnnl.gov/dataset/CEDS-4-21-21>

642 GFEI v2 for the methane emissions from fuel exploitation is available at:
643 <https://dataverse.harvard.edu/dataset.xhtml?persistentId=doi:10.7910/DVN/HH4EUM>
644 [&version=2.0](https://dataverse.harvard.edu/dataset.xhtml?persistentId=doi:10.7910/DVN/HH4EUM)

645 MODIS daily 10km AOD data can be downloaded through NASA Earthdata portal:
646 <https://search.earthdata.nasa.gov/search>

647 DECSO total anthropogenic NO_x emission is available at: www.globemission.eu

648 The CH₄ plume complexes detected by EMIT instrument are available at:
649 <https://earth.jpl.nasa.gov/emit/data/data-portal/Greenhouse-Gases/>

650 **Reference**

651 Abdoli, M., Rezaei, M., & Hasanian, H., 2016. Integrated solid waste management in
652 megacities. *Global Journal of Environmental Science and Management*, 2(3), 289-298.
653 doi: 10.7508/gjesm.2016.03.008

654 Beirle, S., C. Borger, S. Dörner, A. Li, Z. Hu, F. Liu, Y. Wang, and T. Wagner (2019),
655 Pinpointing nitrogen oxide emissions from space, *Science Advances*, 5(11), eaax9800.

656 [Beirle, S., Borger, C., Jost, A. and Wagner, T., 2023. Improved catalog of NOx point
657 source emissions \(version 2\). *Earth System Science Data Discussions*, 2023, pp.1-37.](#)
658 [de Foy, B., Schauer, J.J., Lorente, A. and Borsdorff, T., 2023. Investigating high
659 methane emissions from urban areas detected by TROPOMI and their association with
660 untreated wastewater. *Environmental Research Letters*, 18\(4\), p.044004.](#)

661
662 [Brodrick, P. G., Thorpe, A. K., Villanueva, C. S., Elder, C., Fahlen, J., and Thompson,
663 D. R., 2023. EMIT Greenhouse Gas Algorithms: Greenhouse Gas Point Source
664 Mapping and Related Products, version 1.0, JPL D-107866, EMIT GHG ATBD.](#)

665 Chen, Z., Jacob, D. J., Gautam, R., Omara, M., Stavins, R. N., Stowe, R. C., Nesser, H.,
666 Sulprizio, M. P., Lorente, A., Varon, D. J., Lu, X., Shen, L., Qu, Z., Pendergrass, D. C.,
667 and Hancock, S.: Satellite quantification of methane emissions and oil–gas methane
668 intensities from individual countries in the Middle East and North Africa: implications
669 for climate action, *Atmos. Chem. Phys.*, 23, 5945–5967, [https://doi.org/10.5194/acp-
670 23-5945-2023](https://doi.org/10.5194/acp-23-5945-2023), 2023.

671 Crippa, M., Guizzardi, D., Banja, M., Solazzo, E., Muntean, M., Schaaf, E., Pagani, F.,
672 Monforti-Ferrario, F., Olivier, J., Quadrelli, R., Risquez Martin, A., Taghavi-Moharamli,
673 P., Grassi, G., Rossi, S., Jacome Felix Oom, D., Branco, A., San-Miguel-Ayanz, J. and
674 Vignati, E., CO2 emissions of all world countries – JRC/IEA/PBL 2022 Report, EUR
675 31182 EN, Publications Office of the European Union, Luxembourg,
676 2022, [doi:10.2760/730164](https://doi.org/10.2760/730164), JRC130363.

677 de Gouw, J.A., Veeffkind, J.P., Roosenbrand, E., Dix, B., Lin, J.C., Landgraf, J., Levelt,
678 P.F., 2020. Daily Satellite Observations of Methane from Oil and Gas Production
679 Regions in the United States. *Scientific Reports* 10(1), 1379.
680 <https://doi.org/10.1038/s41598-020-57678-4>.

681 Ding, J., van der A, R. J., Eskes, H. J., Mijling, B., Stavrakou, T., van Geffen, J. H.
682 G. M., Levelt, P. F., 2020. NOx emissions reduction and rebound in China due to the
683 COVID-19 crisis. *Geophysical Research Letters*, 46,
684 e2020GL089912. <https://doi.org/10.1029/2020GL089912>

685 Dlugokencky, E.J., Bruhwiler, L., White, J.W.C., Emmons, L.K., Novelli, P.C.,
686 Montzka, S.A., Masarie, K.A., Lang, P.M., Crotwell, A.M., Miller, J.B., Gatti, L.V.,
687 2009. Observational constraints on recent increases in the atmospheric CH4 burden.
688 *Geophysical Research Letters* 36(18).
689 <https://doi.org/https://doi.org/10.1029/2009GL039780>.

690 Dubey L, Cooper J, Hawkes A. Minimum detection limits of the TROPOMI satellite

691 sensor across North America and their implications for measuring oil and gas methane
692 emissions. *Sci Total Environ.* 2023 May 10;872:162222. doi:
693 10.1016/j.scitotenv.2023.162222. Epub 2023 Feb 14. PMID: 36796684.

694 Eyring, V., N.P. Gillett, K.M. Achuta Rao, R. Barimalala, M. Barreiro Parrillo, N.
695 Bellouin, C. Cassou, P.J. Durack, Y. Kosaka, S. McGregor, S. Min, O. Morgenstern,
696 and Y. Sun, 2021: Human Influence on the Climate System. In *Climate Change 2021:
697 The Physical Science Basis. Contribution of Working Group I to the Sixth Assessment
698 Report of the Intergovernmental Panel on Climate Change*[Masson-Delmotte, V., P.
699 Zhai, A. Pirani, S.L. Connors, C. Péan, S. Berger, N. Caud, Y. Chen, L. Goldfarb, M.I.
700 Gomis, M. Huang, K. Leitzell, E. Lonnoy, J.B.R. Matthews, T.K. Maycock, T.
701 Waterfield, O. Yelekçi, R. Yu, and B. Zhou (eds.)]. Cambridge University Press,
702 Cambridge, United Kingdom and New York, NY, USA, pp. 423–552,
703 doi:10.1017/9781009157896.005.

704 Food and Agriculture Organization of the United Nations (FAO).
705 <https://www.fao.org/home/en/>

706 [United States Geological Survey: Land Cover Products – Global Land Cover](https://doi.org/10.5066/F7GB230D)
707 [Characterization \(GLCC\), https://doi.org/10.5066/F7GB230D, 2018a.](https://doi.org/10.5066/F7GB230D)

708 [United States Geological Survey: Digital Elevation - Global Multi-resolution Terrain](https://doi.org/10.5066/F7J38R2N)
709 [Elevation Data 2010 \(GMTED2010\), https://doi.org/10.5066/F7J38R2N, 2018b.](https://doi.org/10.5066/F7J38R2N)

710 Guo, J., Zhang, J., Yang, K., Liao, H., Zhang, S., Huang, K., Lv, Y., Shao, J., Yu, T.,
711 Tong, B., Li, J., Su, T., Yim, S. H. L., Stoffelen, A., Zhai, P., and Xu, X.: Investigation
712 of near-global daytime boundary layer height using high-resolution radiosondes: first
713 results and comparison with ERA5, MERRA-2, JRA-55, and NCEP-2 reanalyses,
714 *Atmos. Chem. Phys.*, 21, 17079–17097, <https://doi.org/10.5194/acp-21-17079-2021>,
715 2021.

716 Inness, A., Ades, M., Agustí-Panareda, A., Barré, J., Benedictow, A., Blechschmidt,
717 A.M., Dominguez, J.J., Engelen, R., Eskes, H., Flemming, J., Huijnen, V., Jones, L.,
718 Kipling, Z., Massart, S., Parrington, M., Peuch, V.H., Razinger, M., Remy, S., Schulz,
719 M., Suttie, M., 2019. The CAMS reanalysis of atmospheric composition. *Atmos. Chem.*
720 *Phys.* 19(6), 3515-3556. <https://doi.org/10.5194/acp-19-3515-2019>.

721 International Energy Agency (IEA) data and statistics (2021). [https://www.iea.org/data-](https://www.iea.org/data-and-statistics)
722 [and-statistics.](https://www.iea.org/data-and-statistics)

723 Jacob, D. J., Turner, A. J., Maasackers, J. D., Sheng, J., Sun, K., Liu, X., et al. (2016).
724 Satellite observations of atmospheric methane and their value for quantifying methane
725 emissions. *Atmos. Chem. Phys.*, 16(22), 14371-14396. doi:10.5194/acp-16-14371-2016

726 Jacob, D. J., Varon, D. J., Cusworth, D. H., Dennison, P. E., Frankenberg, C., Gautam,

727 R., et al. (2022). Quantifying methane emissions from the global scale down to point
728 sources using satellite observations of atmospheric methane. *Atmospheric Chemistry
729 and Physics*, 22(14), 9617-9646. doi:10.5194/acp-22-9617-2022

730 K. Sims, Fluid flow tutorial, 2018. Available: [https:// www.karlsims.com/fluid-
731 flow.html](https://www.karlsims.com/fluid-flow.html).

732 Lauvaux, T., Giron, C., Mazzolini, M., d'Aspremont, A., Duren, R., Cusworth, D.,
733 Shindell, D., Ciais, P., 2022. Global assessment of oil and gas methane ultra-emitters.
734 *Science* 375(6580), 557-561. <https://doi.org/doi:10.1126/science.abj4351>.

735 Liu, M., van der A, R., van Weele, M., Eskes, H., Lu, X., Veefkind, P., de Laat, J.,
736 Kong, H., Wang, J., Sun, J., Ding, J., Zhao, Y., Weng, H., 2021. A new divergence
737 method to quantify methane emissions using observations of Sentinel-5P
738 TROPOMI. *Geophysical Research Letters*, 48,
739 e2021GL094151. <https://doi.org/10.1029/2021GL094151>

740 Liu, Y., Hu, C., Zhan, W., Sun, C., Murch, B., Ma. L., 2018. Identifying industrial heat
741 sources using time-series of the VIIRS Nightfire product with an object-oriented
742 approach. *Remote Sens. Environ.*, 204, pp. 347-365.
743 <https://doi.org/10.1016/j.rse.2017.10.019>

744 Mijling, B., & van der A, R. J., 2012. Using daily satellite observations to estimate
745 emissions of short-lived air pollutants on a mesoscopic scale. *Journal of Geophysical
746 Research*, 117, D17302. <https://doi.org/10.1029/2012JD017817>

747

748 O'Rourke, Patrick, Smith, Steven J, Mott, Andrea R, Ahsan, Hamza, Mcduffie, Erin E,
749 Crippa, Monica, Klimont, Zbigniew, Mcdonald, Brian, Wang, Shuxiao, Nicholson,
750 Matthew B, Hoesly, Rachel M, and Feng, Leyang. *CEDS v_2021_04_21 Gridded
751 emissions data*. United States: N. p., 2021. Web.
752 doi:10.25584/PNNLDataHub/1779095.

753 Pandey, S., Gautam, R., Houweling, S., van der Gon, H.D., Sadavarte, P., Borsdorff, T.,
754 Hasekamp, O., Landgraf, J., Tol, P., van Kempen, T., Hoogeveen, R., van Hees, R.,
755 Hamburg, S.P., Maasackers, J.D., Aben, I., 2019. Satellite observations reveal extreme
756 methane leakage from a natural gas well blowout. *Proceedings of the National
757 Academy of Sciences* 116(52), 26376. <https://doi.org/10.1073/pnas.1908712116>.

758 Pazoki M, Maleki Delarestaghi R, Rezvanian M R, Ghasemzade R, Dalaei P. Gas
759 Production Potential in the Landfill of Tehran by Landfill Methane Outreach Program.
760 *Jundishapur J Health Sci*. 2015;7(4):e29679. <https://doi.org/10.17795/jjhs-29679>.

761 Rigby, M., Prinn, R.G., Fraser, P.J., Simmonds, P.G., Langenfelds, R.L., Huang, J.,
762 Cunnold, D.M., Steele, L.P., Krummel, P.B., Weiss, R.F., O'Doherty, S., Salameh, P.K.,

763 Wang, H.J., Harth, C.M., Mühle, J., Porter, L.W., 2008. Renewed growth of
764 atmospheric methane. *Geophysical Research Letters* 35(22).
765 <https://doi.org/https://doi.org/10.1029/2008GL036037>.

766 Saunio, M., Stavert, A. R., Poulter, B., Bousquet, P., Canadell, J. G., Jackson, R. B.,
767 Raymond, P. A., Dlugokencky, E. J., Houweling, S., Patra, P. K., Ciais, P., Arora, V. K.,
768 Bastviken, D., Bergamaschi, P., Blake, D. R., Brailsford, G., Bruhwiler, L., Carlson, K.
769 M., Carrol, M., Castaldi, S., Chandra, N., Crevoisier, C., Crill, P. M., Covey, K., Curry,
770 C. L., Etiope, G., Frankenberg, C., Gedney, N., Hegglin, M. I., Höglund-Isaksson, L.,
771 Hugelius, G., Ishizawa, M., Ito, A., Janssens-Maenhout, G., Jensen, K. M., Joos, F.,
772 Kleinen, T., Krummel, P. B., Langenfelds, R. L., Laruelle, G. G., Liu, L., Machida, T.,
773 Maksyutov, S., McDonald, K. C., McNorton, J., Miller, P. A., Melton, J. R., Morino, I.,
774 Müller, J., Murguia-Flores, F., Naik, V., Niwa, Y., Noce, S., O'Doherty, S., Parker, R. J.,
775 Peng, C., Peng, S., Peters, G. P., Prigent, C., Prinn, R., Ramonet, M., Regnier, P., Riley,
776 W. J., Rosentreter, J. A., Segers, A., Simpson, I. J., Shi, H., Smith, S. J., Steele, L. P.,
777 Thornton, B. F., Tian, H., Tohjima, Y., Tubiello, F. N., Tsuruta, A., Viovy, N.,
778 van der A, R. J., Ding, J., and Eskes, H.: Monitoring European anthropogenic NOx
779 emissions from space, *EGUsphere* [preprint], [https://doi.org/10.5194/egusphere-2023-](https://doi.org/10.5194/egusphere-2023-3099)
780 [3099](https://doi.org/10.5194/egusphere-2023-3099), 2024

781 Voulgarakis, A., Weber, T. S., van Weele, M., van der Werf, G. R., Weiss, R. F., Worthy,
782 D., Wunch, D., Yin, Y., Yoshida, Y., Zhang, W., Zhang, Z., Zhao, Y., Zheng, B., Zhu,
783 Q., Zhu, Q., and Zhuang, Q.: The Global Methane Budget 2000–2017, *Earth Syst. Sci.*
784 *Data*, 12, 1561–1623, <https://doi.org/10.5194/essd-12-1561-2020>, 2020.

785 Scarpelli, T. R., Jacob, D. J., Grossman, S., Lu, X., Qu, Z., Sulprizio, M. P., Zhang, Y.,
786 Reuland, F., Gordon, D., and Worden, J. R.: Updated Global Fuel Exploitation
787 Inventory (GFEI) for methane emissions from the oil, gas, and coal sectors: evaluation
788 with inversions of atmospheric methane observations, *Atmos. Chem. Phys.*, 22, 3235–
789 3249, <https://doi.org/10.5194/acp-22-3235-2022>, 2022.

790 Schneider, A., Borsdorff, T., aan de Brugh, J., Aemisegger, F., Feist, D.G., Kivi, R.,
791 Hase, F., Schneider, M., Landgraf, J., 2020. First data set of H₂O/HDO columns from
792 the Tropospheric Monitoring Instrument (TROPOMI). *Atmos. Meas. Tech.* 13(1), 85-
793 100. <https://doi.org/10.5194/amt-13-85-2020>.

794

795 Schneising, O., Buchwitz, M., Hachmeister, J., Vanselow, S., Reuter, M., Buschmann,
796 M., Bovensmann, H., and Burrows, J. P.: Advances in retrieving XCH₄ and XCO from
797 Sentinel-5 Precursor: improvements in the scientific TROPOMI/WFMD algorithm,
798 *Atmos. Meas. Tech.*, 16, 669–694, <https://doi.org/10.5194/amt-16-669-2023>, 2023.

799 [Sun, K., 2022. Derivation of Emissions From Satellite-Observed Column Amounts and](#)

800 [Its Application to TROPOMI NO₂ and CO Observations. *Geophysical Research*](#)
801 [Letters, 49\(23\), p.e2022GL101102.](#)

802

803 Turner, A.J., Frankenberg, C., Kort, E.A., 2019. Interpreting contemporary trends in
804 atmospheric methane. *Proceedings of the National Academy of Sciences* 116(8), 2805.
805 <https://doi.org/10.1073/pnas.1814297116>.

806 Varon, D. J., Jervis, D., McKeever, J., Spence, I., Gains, D., and Jacob, D. J.: High-
807 frequency monitoring of anomalous methane point sources with multispectral Sentinel-
808 2 satellite observations, *Atmos. Meas. Tech.*, 14, 2771–2785,
809 <https://doi.org/10.5194/amt-14-2771-2021>, 2021.

810 Veefkind, J.P., Aben, I., McMullan, K., Förster, H., de Vries, J., Otter, G., Claas, J.,
811 Eskes, H.J., de Haan, J.F., Kleipool, Q., van Weele, M., Hasekamp, O., Hoogeveen, R.,
812 Landgraf, J., Snel, R., Tol, P., Ingmann, P., Voors, R., Kruizinga, B., Vink, R., Visser,
813 H., Levelt, P.F., 2012. TROPOMI on the ESA Sentinel-5 Precursor: A GMES mission
814 for global observations of the atmospheric composition for climate, air quality and
815 ozone layer applications. *Remote Sensing of Environment* 120, 70-83.
816 <https://doi.org/https://doi.org/10.1016/j.rse.2011.09.027>.

817 Veefkind, J. P., Serrano-Calvo, R., de Gouw, J., Dix, B., Schneising, O., Buchwitz,
818 M., Barré, J., van der A, R.J., Liu, M., Levelt, P.F., 2023. Widespread frequent methane
819 emissions from the oil and gas industry in the Permian basin. *Journal of Geophysical*
820 *Research: Atmospheres*, 128,
821 e2022JD037479. <https://doi.org/10.1029/2022JD037479>

822 Zhang, Y., Gautam, R., Pandey, S., Omara, M., Maasackers, J.D., Sadavarte, P., Lyon,
823 D., Nesser, H., Sulprizio, M.P., Varon, D.J., Zhang, R., Houweling, S., Zavala-Araiza,
824 D., Alvarez, R.A., Lorente, A., Hamburg, S.P., Aben, I., Jacob, D.J., 2020. Quantifying
825 methane emissions from the largest oil-producing basin in the United States from space.
826 *Science Advances* 6(17), eaaz5120. <https://doi.org/10.1126/sciadv.aaz5120>.

827